Journal of Materials Chemistry A

Accepted Manuscript

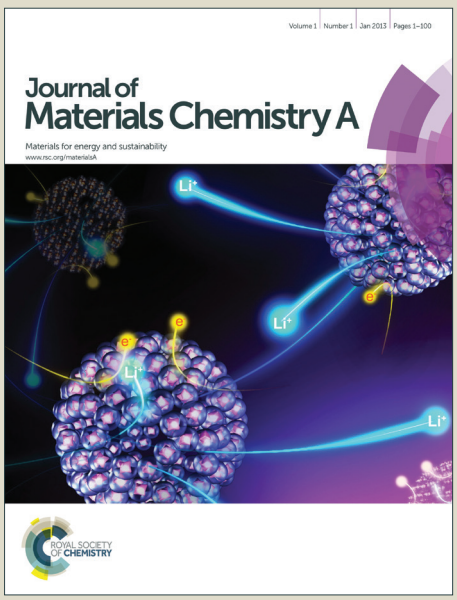

ROYAL SOCIETY OF CHEMISTRY

www.rsc.org/materialsA

Journal of Materials Chemistry A

Dynamic Article Links ►

Cite this: DOI: 10.1039/c0xx00000x

ARTICLE TYPE

www.rsc.org/xxxxxx

One-Pot Synthesis of Carbon Nanoribbons and their enhanced lithium storage performance

Tao Mei,*[a] Liu Zhang,[a] Xianbao Wang*[a] and Yitai Qian[b]

Received (in XXX, XXX) Xth XXXXXXXXX 20XX, Accepted Xth XXXXXXXXX 20XX

DOI: 10.1039/b000000x

Carbon nanoribbons are obtained on a large scale by an easy one-pot pathway. The nanoribbons with thickness of ~5 nm, width of ~500 nm together with a length longer than 15 μm are prepared starting from ferrocene and $Mg(CH_3COO)_2{\cdot}4H_2O$ at 600 °C for 10 h. Raman spectrum indicates that the as-obtained sample possesses a mass of disorder and defects. XPS result shows the nanoribbins are doped by nitrogen with the atomic percentage as 2.09 %. The specific surface area of the sample is measured to be as large as 1240 m^2/g. In the charge/discharge experiments of secondary lithium ion batteries, the carbon nanoribbons demonstrate a stable reversible capacity of 750 mAh/g after 300 cycles at 0.5 A/g, which suggest the potential application of the as-prepared carbon nanoribbons as electrode material in electronic devices.

1. Introduction

Two-dimensional (2-D) carbon nanoribbons have received considerable attention in both academia and industry due to their unique properties depending on the geometry, in particular, high aspect ratio and low percolation threshold [1]. However, the synthesis of graphite 2-D nanosheets, especially for high aspect ratio nanoribbons, is mainly limited due to their intrinsic instability which has the notorious tendency to curve into tube structures or to stack by polarization interactions. Carbon nanoribbons with average diameters larger than 15μm are rarely produced. Therefore, developing easy, inexpensive, and scalable methods for preparing nanoribbons is the key to the exploration of the potential applications of such materials. Recently, several lithographic [2], chemical [3] and synthetic procedures [4-7] are known to produce microscopic samples of carbon nanoribbons. For instance, chemical vapor deposition process successfully produced macroscopic quantities of nanoribbons at 950 °C [4]. Semi-cylindrical carbon nanoribbons were prepared based on the carbonization of in situ formed fibrous polymer precursors at 900 °C [8]. A solution-based oxidative process was used to produce nanoribbon structures by lengthwise cutting and unravelling of multiwalled carbon nanotube side walls [9]. Carbon nanoribbons were also obtained from graphite electrode using ionic liquid-assisted electrochemical exfoliation [10]. Ribbon-like activated carbon was developed by a two-step activation process based on alkali activation and an electrochemical activation route [11] and so on.

As a mainstream anode material for lithium ion batteries, graphite can be reversibly charged and discharged with a theoretical capacity of 372 mAh/g. The nano-structural materials which have large specific surface area and micro-porous structure can greatly increase the electrode/electrolyte contact area, accommodate the electrode structural deformation and shorten the diffusion path of current carriers. Recently, different nano-structural carbon materials have been utilized as the electrode materials for rechargeable lithium-ion battery anodes [12, 13]. Among them, 2-D nanostructures in many cases have specific good performance to overcome the problems such as a limited specific capacity and fast capacity fade. Great efforts have been made to increase electrochemical performance by altering the carbon structures, increasing lattice disordering, and increasing surfaces areas. For example, it was reported that graphene nanosheets could exhibit a specific capacity of 540 mAh/g when they were used in the charge/discharge experiments of secondary lithium ion batteries [14]. At a current density of 100 mA/g, the first reversible specific capacity of the prepared graphene sheets with specific surface area of 493 m^2/g was 1264 mAh/g, the reversible capacity was kept at 848 mAh/g after 40 cycles [15]. Graphene nanoribbons with diameters of ~50 nm obtained by unzipping pristine multiwalled carbon nanotubes presented a first charge capacity of ~1400 mAh/g, together with a reversible capacity of 800 mAh/g and a capacity loss per cycle of ~3 % for early cycles and a decreasing loss rate for subsequent cycles (500 mAh/g at 14th cycle) [16].

In this study, we reported an easy one-pot pathway for the large-scale preparation of carbon nanoribbons. The thickness of the nanoribbons was ~5 nm, together with a high aspect ratio larger than 300, which demonstrated a stable reversible capacity of 750 mAh/g after 300 cycles at 0.5 A/g. It was envisaged that the unique 2D nanostructure, large surface area and appropriate nitrogen doping are favorable for the improved Li-storage capacity and good cycling stability.

2. Experimental section

All the chemical reagents used here were analytical grade, purchased from Shanghai Chemical Industrial Corp and used as received without further purification. The autoclave are

manufactured by Anhui Kelan Experiment Instrument Euipment Co., LTD. In a typical synthesis process, 2.0 g $Mg(CH_3COO)_2 \cdot 4H_2O$ and 0.5 g ferrocene were weighed and mixed by grinding in a mortar for about 15 min until well-blended, and then were placed into a stainless-steel autoclave of 20 mL capacity. The autoclave was sealed and put into an electronic furnace from room temperature with an increasing speed of 10 °C/min to 600 °C then maintained at 600 °C for 10 h, after that it was cooled to room temperature naturally. In order to remove the byproducts, the precipitates in the autoclave were collected and firstly put into a beaker with 200 mL 10 wt. % hot nitric acid (60 °C), keeping stirring for 12 h, and then were washed by deionized water and absolute ethanol several times till the pH of the filtrate was about 7. After that, the products were dried in a vacuum at 60 °C for 5 h for further characterization.

X-ray powder diffraction (XRD) patterns of the products were recorded on a Philips X'pert X-ray diffractometer with Cu Ka radiation (λ = 1.54182 Å). The microstructure was observed on a transmission electron microscope (TEM, H7650) and a field-emitting scanning electron microscope (SEM, JEOL-JSM-6700F). Raman spectrum was carried out on a JY LABRAM-HR confocal laser micro-Raman spectrometer using Ar^+ laser excitation with a wavelength of 514.5 nm. The Brunauer–Emmett–Teller (BET) surface area was measured on a Micrometrics ASAP 2020 accelerated surface area and porosimetry system. The pore size distribution (PSD) was calculated via a density functional theory (DFT) method by using nitrogen adsorption data and assuming a slit pore model (ASAP 2020 V3.01). XPS were recorded on an ESCALAB 250 spectrometer (Perkin-Elmer) to characterize the surface composition.

Charge / discharge tests were carried out using coin-type cells (size: 2016), which consisted of an active material working electrode and a Li foil counter electrode separated by a Celgard 2300 microporous membrane. To prepare the working electrode, active material and polyvinylidene fluoride (PVDF) were mixed by the weight ratio of 9:1 with N-methyl pyrrolidone (NMP) serving as the solvent to obtain a slurry. After coating the slurry onto a copper foil current collector, the electrode was dried at 120 °C in vacuum for 12 h. Typical loadings of the electrodes were between 2 and 3 mg of active material. 1 mol/L solution of $LiPF_6$ dissolved in ethylene carbonate/dimethyl carbonate (EC/DMC) (1:1 volume ratio) was used as the electrolyte. The cells were assembled in an argon-filled glove box (Mikrouna, Super 1220/750/900, China) and then charged/discharged galvanostatically from 3.0 to 0.01 V versus Li^+/Li at current densities of 0.5 A/g on a LAND CT2001A battery test system. It should be noted that the specific capacity was calculated on the mass of the active materials(C+N). Cyclic voltammetry (CV) was performed at a scanning rate of 0.1 mV/s between 0.001 and 3.00 V (vs Li^+/Li) at room temperature by an electrochemical workstation (CHI660D) .

3. Results and discussion

Fig. 1a shows the typical XRD pattern of the as-obtained carbon nanoribbons. It shows two peaks, the broad diffraction peak around 25.5° corresponding to the (002) diffraction of the graphitic layer-by-layer structure. The other distinct diffraction peak with d-spacing of 2.040 could be indexed as the diffraction of (101) from hexagonal graphite (JCPDS card no. 41-1487). The Raman spectra of carbon nanoribbons are shown in Fig. 1b. There are two bands at 1357 and 1586 cm^{-1}, which are typical bands of carbon nominated as the D band and G respectively. The D band, corresponding to the vibration of carbon atoms with dangling bonds in-plane terminations of disordered graphite, is associated with edge defects, and other defects such as sp^3 bond carbon, dangling bonds, topological defects and vacancies. While the G bond corresponds to the Raman-allowed optical mode E2g, which is closely related to the vibration of sp^2-bonded carbon atoms in a 2D hexagonal lattice [12], The ID/IG value of the sample is 0.85, indicating that the as-obtained sample possesses a mass of disorder and defects which could provide more lithium storage sites.

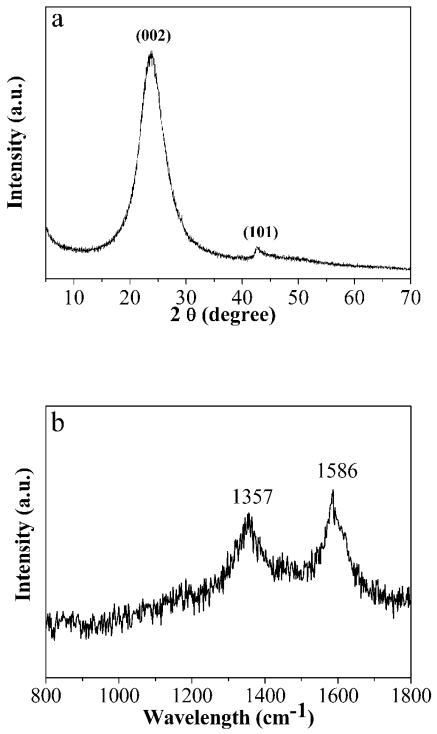

Fig. 1 (a) Typical XRD pattern and (b) the typical Raman spectrum of the carbon nanoribbons.

The morphology of the as-prepared carbon nanoribbons are further analyzed by SEM, TEM and HRTEM. Fig. 2a and 2b show the typical SEM images of the as-obtained sample, in which high proportion of carbon nanoribbons is observed. Fig. 2a exhibits characteristic transparent gossamer ribbons with wavy and crumpled structures. From Fig. 2b, it could be seen that the width of the carbon nanoribbons is up to ~500 nm. Moreover, from the wrinkled place which contains two-layer nanoribbons, it could presume that the thickness of the carbon nanoribbons is ca. 5 nm. From the TEM image (Fig. 2c), we can see that high proportion of carbon nanoribbons too, which are intertwined with each other to form a network structure. Besides, the length of the carbon nanoribbons is longer than 15 μm. The HRTEM in Fig. 2d is taken by the warped edge of one nanoribbon which confirms

that the thickness of gossamer ribbons is about 5 nm. The observation results of the SEM and TEM images indicate that these carbon nanoribbons have a high aspect ratio, uniform shapes and a tendency to come out wrinkled.

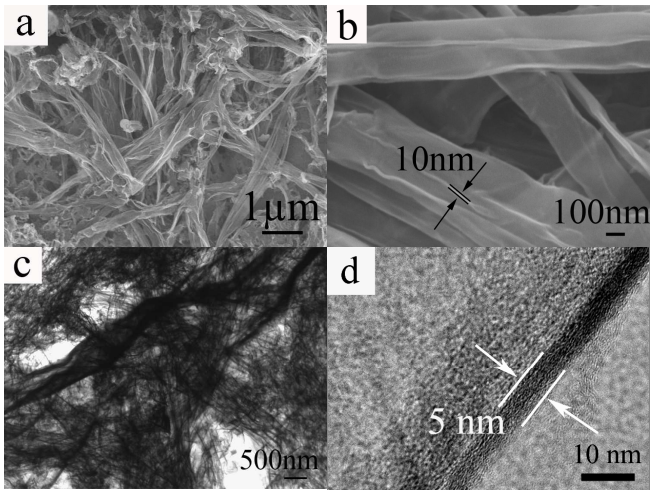

Fig. 2 (a, b) Typical SEM images, (c) TEM image and (d) HRTEM image of carbon nanoribbons.

The BET specific surface area and pore size distribution of carbon nanoribbons are determined from the nitrogen adsorption/desorption isotherm (Fig. 3), which exhibits IV type characteristics. The curve of the sample displays a hysteresis loop at a relative pressure (P/P_o)≈0.4-1.0, which means that the resultant product may possesses framework structures. Meanwhile, the large volume adsorbed at the lower P/Po=0-0.2 suggests the presence of lots of microporosity. The BET specific surface area of the nanoribbon is 1240 m^2/g, which is higher than that of previously reported natural graphite (1.7-6.0 m^2/g) and expanded graphite (40-60 m^2/g). At the same time, Pore size distribution of nanoribbons is analyzed based on the density functional theory (DFT) method. The inset of Fig. 3 demonstrates that the pore size of the nanoribbons is concentrated in the range of 5-10 nm. It could be seen that among them more than 70% is around 5 nm which is consistent with the thickness of the nanoribbons.

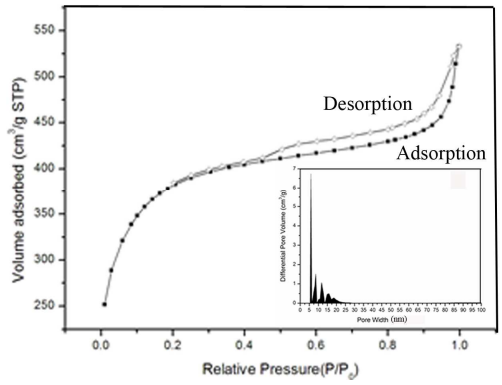

Fig. 3 Nitrogen adsorption/desorption isotherm of carbon nanoribbons, the inset is the pore size distribution based on DFT method.

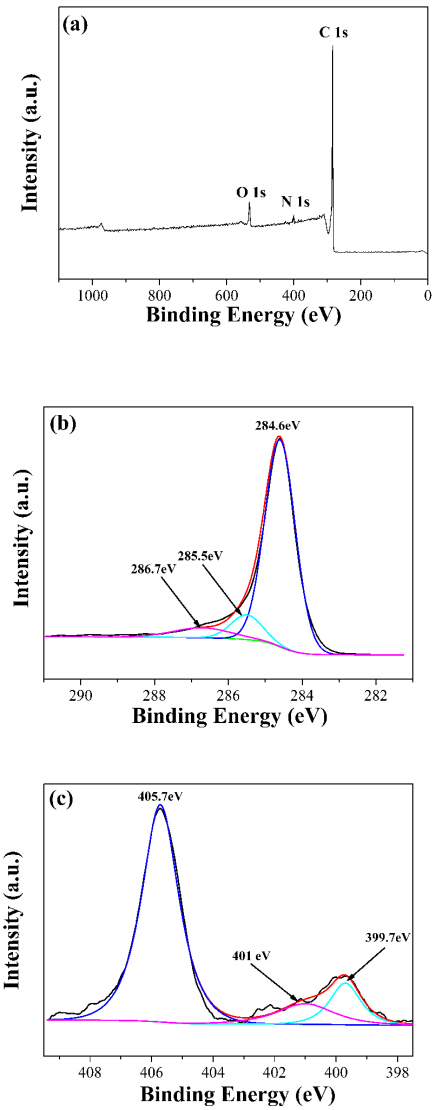

Fig. 4 XPS spectra of the carbon nanoribbons: survey (a), C1s (b) and N1s (c).

The surface chemical properties of the as-obtained carbon nanoribbons are further analyzed by XPS. Fig. 4a exhibits the survey spectrum (0-1100 eV) of the carbon nanoribbons, it basically reveals the evidence for the content of carbon, oxygen, and nitrogen species which are 91.46, 6.45, and 2.09 at.-%, respectively and without any other impurities, From Fig. 4b, it can be seen the C1s spectrum ranging from 281 to 296 eV which is slightly asymmetric in shape. After carefully being fitted toward C1s, it can be divided into three obvious peaks centering at ca. 284.6, 285.5 and 286.7 eV. Usually, the binding energy at ca. 284.6 eV can be attributed to sp^2 C-C bonds, ca. 285.5 eV assignable to N-sp^2 C bonds, while ca. 286.7 eV corresponding to N-sp^3 C bonds [17]. In Fig. 4c, the N1s spectrum shows a wide peak ranging from 398 to 408 eV which also can be divided into three peaks centering at ca. 399.7, 401.0 and 405.7 eV. In the previous reports [18, 19], the distribution of nitrogen functional forms in nitrogen-containing carbon materials changes according to the

specific preparation condition and method. Usually, there are several kinds of nitrogen species which including pyridinic nitrogen (398.6 ± 0.3 eV), pyrrolic nitrogen (400.1 ± 0.3 eV), graphitic nitrogen (401.3±0.3 eV), oxided pyridinic nitrogen (402-405 eV) and nitro-typed nitrogen at binding energies above 405 eV. According to above information, the peak at ca. 399.7, 401.0 and 405.7 eV belongs to pyrrolic nitrogen, graphitic nitrogen and nitro-typed nitrogen, respectively. It was reported that the nitrogen atoms incorporated in the carbon-based materials could generate plenty of defects and withdraw electrons from carbon atoms due to the higher electronegativity of N, which is expected to improve the kinetics of lithium diffusion and transfer, beneficial to the electrochemical performance [20-23].

On the basis of experimental results, the possible growth mechanism for carbon nanoribbons and why these 2-D nanostructures could exist stably might be as follows: firstly, with the increase of the reaction temperature, the initial raw materials began decomposition and gasification, carbonaceous gas cracked on the metallic surface, and then after reaching a certain concentration of carbon atoms on the metallic surface, nucleation process is triggered, finally, the further growth of crystal nucleus result in continuous graphite layer to form carbon nanoribbons. Exactly to say, the observation results of the SEM and TEM images indicate that these carbon nanoribbons have a tendency to come out wrinkled, just like why graphene could exist stably at room temperature, the ripples and the puddles on the this kind of materials' surface usually helpful to stabilize the 2-D structure [24-27]. On the other hand, graphite has the notorious tendency to stack due to its polarization interactions, except when the surface is sufficiently oxidized (such as graphene oxide). XPS supports this view which find suffcient amounts of oxygen, as well as indications for the incorporation of nitrogen.

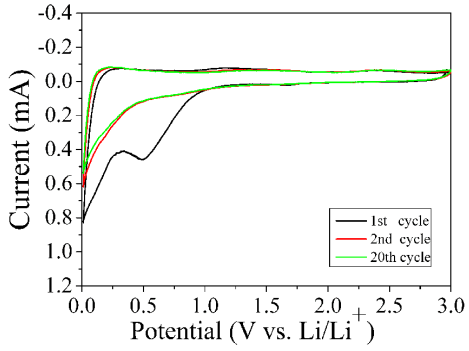

Fig. 5 Cyclic voltammograms of carbon nanoribbon based electrode at a scan rate of 0.1 mV/s.

Coin-type cells are assembled to evaluate the electrochemical performance of the carbon nanoribbon based electrode. Fig. 5 shows the first, second and the 20th cyclic voltammograms of freshly electrode between 3.0 and 0.001 V at a scanning rate of 0.1 mV/s, which exhibits typical CV curves of the carbonaceous anode materials. On the first cycle, the broad reduction peak at about 0.6 V can be attributed to the preliminary decomposition of electrolytes, the formation of solid electrolyte interface (SEI) films [28]and the reaction of lithium ions with the residual acid [29]. The peak disappears in the second cycle, which means that the surface of nanoribbons is passivated during the first cycle. The peaks close to 0 V are observed in all the CV curves resulting from Li^+ intercalation into the carbon based anodes [30]. Also, all of the anodic curves of the carbon nanoribbon based electrode almost overlap with each other, implying the reversible oxidation of some SEI components and considerable cycling stability.

Fig. 6a shows the first and the 300th charge-discharge cycles of as-obtained carbon nanoribbons at a rate of 0.5 A/g between 0.01 and 3.00 V. The initial charge and discharge capacities at the first cycle are 1111 and 1325 mAh/g, with a high coulombic efficiency of 83.8 %. It is worthy to note that the coulombic efficiency at the first cycle is high which could attribute to the following reasons: i) the network structure ensure the fast and continuous electronic conductivity which leads to an effective percolation of the current collecting phases, finally result in forming uniform and thin SEI films, ii) the thickness of nanoribbon is about 5 nm, the diffusion length for mass transport decreases significantly, which leads to helpful mass trasport properties facilitating Li insertion and structural rearrangement [31]. The initial capacity for the carbon nanoribbons is more than 3.5 times higher than that of pure carbon, which imply that there should be some other lithium storage routes existing in carbon nanoribbons except the conventional graphite intercalation mechanism [32, 33]. Even after 300 cycles, the charge and discharge capacities are remain 725 and 750 mAh/g, respectively, together with a coulombic efficiency of 96.7 %. On the other hand, it is noting that the charge/discharge curves of carbon nanoribbons display significantly different profiles compared with that of graphite, the slope starts approximately 2.5 V (vs Li/Li+) and has large specific capacities below 0.5 V without distinguishable plateaus, which imply the presence of at least two different Li-storage sites in these carbon nanoribbons. Due to the peculiar sp^2 domain model and the higher specific surface area, in the process of chargeing and dischargeing, lithium ion intercalation and deintercalation occurring in the graphite crystallite. Usually it is not obvious to observe a clear plateaus which attribute to the lithium ion embedding into the graphite layers to form LiC_6 class compounds, instead, present a electrochemical characteristics of gradual rise and decline as well as a voltage hysteresis, similar Li-storage behavior can also be observed in graphene [14] and hard carbon [34]. The capacity of the potential region lower than 0.5 V should be due to lithium intercalation into the carbon nanoribbons, while the absence of a potential plateau suggests a disordered stacking of the carbon nanosheet structures, resulting in electrochemically and geometrically nonequivalent Li^+ sites. Meanwhile, the capacity above 0.5 V may be associated with a faradic capacitance either on the nanoribbons surface or on the edge plane [14].

Fig. 6b shows the cycle life performance of the carbon nanoribbons at a current density of 0.5 A/g. As the cycling continued from the 1st cycle up to the 300th cycle, a significant descrease in the specific capacity is observed from 1325 to 765 mAh/g for the first 12 cycles. However after the 12th cycle, the discharge capacity tend to be relatively stable as about 750 mAh/g. Notably, in order to further test the high rate performance for the carbon nanoribbons anode (Fig. 6c), the cell is discharged/charged at various current densities from 0.1 to 3 A/g

each for 10 cycles (the first 20 cycles are discharged/charged at 0.5A/g). The discharge capacities are 913, 853, 801, 551, 352, and 273 mAh/g at 0.1, 0.2, 0.3, 1, 2 and 3 A/g, respectively. When the rate is tuned back to 0.5 A/g after cycling at different rates, the discharge capacity can be recovered to 748 mAh/g after 150 cycles, implying the good reversibility of the materials.

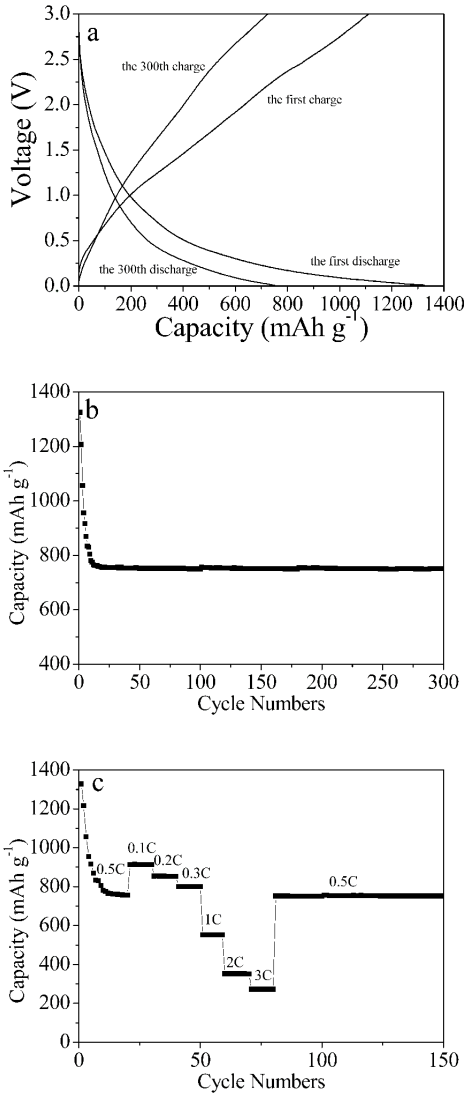

Fig. 6 (a) The typical first and the 300th charge/discharge behavior and (b) the cycle life performances of the as-obtained carbon nanoribbons at a current density of 0.5 A/g, (c) the cycle life performances as the rate varying from 0.1 to 3 A/g (the first 20 cycles are discharged/charged at 0.5A/g).

The good performance of the as-obtained carbon nanoribbons may mainly attribute to the following reasons: The good performance of the as-obtained carbon nanoribbons may mainly attribute to the following reasons: firstly, the thickness of nanoribbon is about 5 nm which could greatly reduce the solid-state transport lengths for Li diffusion, Li^+ could be electrochemically adsorbed on both sides of single nanoribbon that are arranged like "falling cards" (the house-of-cards model) [20]; secondly, not only nanocrystallization, but also the constructions of nanocomposites with high conductivity and activity are helpful to improve electrochemical performance of lithium ion batteries [35]. Such a self-assembled three-dimensional network nanostructure exhibited high conductivity, large specific surface area (1240 m^2/g) and unique porosity which could as the conductive additive and supporting matrix [36]. The interconnected carbon-framework structure ensured the fast and continuous transportation of electrons in the electrode, provided continuous paths between the carbon ribbons, which was favorable for electrons moving unimpeded over active materials to attain a high rate capability [37]; thirdly, as is known, in case of the disordered carbonaceous materials, various models of lithium storage have been put forward to account for the high amount of extra lithium such as storage in cavities or nanopores, vacancies, surfaces and interfaces and the effect of heteroatoms. The defects such as edges and vacancies in the as-obtained nanoribbons could provide more lithium storage sites, contributing to the high reversible capacity [32], moreover, the N doping in carbon nanoribbons can enhance the electrochemical reactivity and electronic conductivity , which makes an additional contribution to the exceptional performance [38]; finally, the activation process of the active materials which can decrease the cell resistance and the growth of a reversible polymer gel-like film or the so-called nanogel caused by the decomposition of the electrolyte. The in situ polymeric layer is believed to enable additional lithium storage on its surface through a so-called "pseudo-capacitance-type behavior", thereby contributing to the extra capacities.

Conclusions

In this work, we report an easy pathway for the large-scale preparation of carbon nanoribbons with thickness of ca. 5 nm. The width of the carbon nanoribbons is up to ~500 nm and the length is longer than 15 μm. The nanoribbons are interconnected with each other to form a unique 3D framework which possesses a specific surface area up to 1240 m^2/g. In the charge/discharge experiments of secondary lithium ion batteries, the nanoribbons show high capacity and stable cyclability at different current densities. The specific capacity is as high as 750 mAh/g after 300 cycles at 0.5 A/g. The significant improvement is due to the fact that the unique thin ribbon structure, the large specific surface area and the appropriate nitrogen introduction. Since the as-obtained carbon nanoribbons exhibit a large BET specific surface area and a good electrochemical performance, further studies to use other electrochemically active materials, such as Si, Sn and the transition metal oxides nanoparticles loading into these carbon nanoribbons are under progress. These updated composites may have more useful and potential applications in Li-ion battery.

Acknowledgements

This work was financially supported by National Natural Science Foundation (No. 51272071) and the 973 Project of China (No. 2011CB935901).

Notes and references

[a] *Hubei Collaborative Innovation Center for Advanced Organic Chemical Materials, Ministry-of-Education Key laboratory for the Green Preparation and Application of Functional Materials, Faculty of Materials Science and Engineering, Hubei University, Wuhan 430062, PR China E-mail: meitao@hubu.edu.cn; wangxb68@aliyun.com; Tel: +86 27 8866 2132.*
[b] *Department of Chemistry, University of Science and Technology of China, Hefei, Anhui 230026, P. R. China*

1. Y. W. Son, M. L. Cohen and S. G. Louie, *Nature,* 2006, **444**, 347.
2. M. Y. Han, B. Ozyilmaz, Y. Zhang and P. Kim, *Phys Rev Lett,* 2007, **98**, 206805.
3. X. Li, X. Wang, L. Zhang, S. Lee and H. Dai, *Science,* 2008, **319**, 1229.
4. J. Campos-Delgado, J. M. Romo-Herrera, X. Jia, D. A. Cullen, H. Muramatsu, Y. A. Kim, T. Hayashi, Z. Ren, D. J. Smith, Y. Okuno, T. Ohba, H. Kanoh, K. Kaneko, M. Endo, H. Terrones, M. S. Dresselhaus and M. Terrones, *Nano Lett,* 2008, **8**, 2773.
5. F. Plasser, H. Pasalic, M. H. Gerzabek, F. Libisch, R. Reiter, J. Burgdorfer, T. Muller, R. Shepard and H. Lischka, *Angew. Chem.-Int. Edit.*, 2013, **52**, 2581.
6. G. Yuan, X. Li, Z. Dong, A. Westwood, B. Rand, Z. Cui, Y. Cong, J. Zhang, Y. Li and Z. Zhang, *Carbon,* 2014, **68**, 426.
7. G. Yuan, X. Li, Z. Dong, X. Xiong, B. Rand, Z. Cui, Y. Cong, J. Zhang, Y. Li and Z. Zhang, *Carbon,* 2014, **68**, 413.
8. S. W. Kim and C. R. Park, *Carbon,* 2009, **47**, 2391.
9. D. V. Kosynkin, A. L. Higginbotham, A. Sinitskii, J. R. Lomeda, A. Dimiev, B. K. Price and J. M. Tour, *Nature,* 2009, **458**, 872.
10. J. Lu, J.-x. Yang, J. Wang, A. Lim, S. Wang and K. P. Loh, *ACS nano,* 2009, **3**, 2367.
11. M.-H. Kim, K.-B. Kim, K. Kang, J. T. Han and Roh, K. C. *J. Mater. Chem. A,* 2013, **1**, 14008.
12. X. W. D. Lou, L. A. Archer and Z. Yang, *Adv. Mater.*, 2008, **20**, 3987.
13. L. Ji, Z. Lin, M. Alcoutlabi and X. Zhang, *Energ. Environ. Sci.*, 2011, **4**, 2682.
14. E. Yoo, J. Kim, E. Hosono, H.-s. Zhou, T. Kudo and I. Honma, *Nano Lett.*, 2008, **8**, 2277.
15. P. Lian, X. Zhu, S. Liang, Z. Li, W. Yang and H. Wang, *Electrochim. Acta,* 2010, **55**, 3909.
16. T. Bhardwaj, A. Antic, B. Pavan, V. Barone and B. D. Fahlman, *J. Am. Chem. Soc.*, 2010, **132**, 12556.
17. A. L. M. Reddy, A. Srivastava, S. R. Gowda, H. Gullapalli, M. Dubey and P. M. Ajayan, *ACS nano,* 2010, **4**, 6337.
18. H. Liu, Y. Zhang, R. Li, X. Sun, S. Désilets, Abou-Rachid, M. Jaidann and L.-S. Lussier, *Carbon,* 2010, **48**, 1498.
19. T. Horikawa, N. Sakao, T. Sekida, J. I. Hayashi, D. Do and M. Katoh, *Carbon*, 2012, **50**, 1833.
20. J. Xue and J. Dahn, *J. Electrochem. Soc.*, 1995, **142**, 3668.
21. R. Czerw, M. Terrones, J.-C. Charlier, X. Blase, B. Foley, R. Kamalakaran, N. Grobert, H. Terrones, D. Tekleab and P. Ajayan, *Nano Lett.,* 2001, **1**, 457.
22. H. Wang, C. Zhang, Z. Liu, L. Wang, P. Han, H. Xu, K. Zhang, S. Dong, J. Yao and G. Cui, *J. Mater. Chem.*, 2011, **21**, 5430.
23. Z.-S. Wu, W. Ren, L. Xu, F. Li and H.-M. Cheng, *ACS nano,* 2011, **5**, 5463.
24. A. Fasolino, J. Los and M. I. Katsnelson, *Nat. mater.* 2007, **6**, 858.
25. A. K. Geim and K. S. Novoselov, *Nat. mater.* 2007, **6**, 183.
26. F. Guinea, B. Horovitz and P. Le Doussal, *Phys. Rev. B* 2008, **77**, 205421.
27. J. Martin, N. Akerman, G. Ulbricht, T. Lohmann, J. Smet, K. Von Klitzing and A. Yacoby, *Nat. Phys.* 2008, **4**, 144.
28. L. Bulusheva, A. Okotrub, A. Kurenya, H. Zhang, H. Zhang, X. Chen and H. Song, *Carbon,* 2011, **49**, 4013.
29. Z. Yang, H.-Q. Wu and B. Simard, *Electrochem. Commun.,* 2002, **4,** 574.
30. X. Li, D. Geng, Y. Zhang, X. Meng, R. Li and X. Sun, *Electrochem. Commun.,* 2011, **13,** 822.
31. Y. Matsumura, S. Wang and J. Mondori, *J. Electrochem. Soc.*, 1995, **142**, 2914.
32. N. A. Kaskhedikar and J. Maier, *Adv. Mater.*, 2009, **21**, 2664.
33. L. Su, Z. Zhou and P. Shen, *J. Phys. Chem. C*, 2012, **116**, 23974.
34. J. Hu, H. Li and X Huang, *Solid S*J. Hu, H. Li and X Huang, *Solid State Ion.* 2007, **178**, 265.
35. C. X. Guo, M. Wang, T. Chen, X. W. Lou and C. M. Li, *Adv. Energy Mater.*, 2011, **1**, 736.
36. S. L. Candelaria, Y. Shao, W. Zhou, X. Li, J. Xiao, J.-G. Zhang, Y. Wang, J. Liu, J. Li and G. Cao, *Nano Energy,* 2012, **1**, 195.
37. F. D. Han, Y. J. Bai, R. Liu, B. Yao, Y. X. Qi, N. Lun and J. X. Zhang, *Adv. Energy Mater.*, 2011, **1**, 798.
38. F. Su, C. K. Poh, J. S. Chen, G. Xu, D. Wang, Q. Li, J. Lin and X.W. Lou, *Energ. Environ. Sci.*, 2011, **4**, 717.

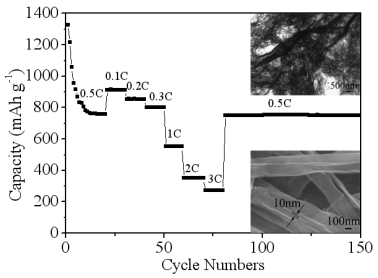

The manuscript reports a new one-pot synthesis of carbon nanoribbons with enhanced lithium storage performances for lithium ion batteries.